



# The formation mechanism and distribution of micro-aluminum oxide layer

Yunan Zhou<sup>1</sup> · Jianzhong Liu<sup>1</sup> · Jianru Wang<sup>2</sup> · Tuanwei Xv<sup>2</sup> · Daolun Liang<sup>1</sup> · Kefa Cen<sup>1</sup>

Received: 1 November 2017 / Accepted: 4 March 2018 / Published online: 31 March 2018  
© Akadémiai Kiadó, Budapest, Hungary 2018

## Abstract

It is of great significance to study the thermal oxidation process to understand the reaction mechanism of aluminum particle and further its applications in propellants. The physical and chemical properties of micron-aluminum particle were evaluated by scanning electron microscopy, laser particle size analyzer, X-ray diffractometer and inductively coupled plasma atomic emission spectrometer. The thermal oxidation characteristics of the sample were studied by thermal analyzer. The experimental results showed that the initial oxide thickness of the sample was about 3.96 nm, and the calculated values of the specific surface area and the active aluminum content obtained by the established mathematical model were in good agreement with the measured values. The thermal oxidation process of the sample was divided into three stages. When the temperature rose to 1100 °C, the thermal oxidation efficiency of the sample reached 98.55%. With the increase in treatment temperature, dramatic crystalline changes occurred on the surface of the sample: amorphous alumina— $\gamma$ -Al<sub>2</sub>O<sub>3</sub>,  $\alpha$ -Al<sub>2</sub>O<sub>3</sub>, and the oxide layer thickness increased from 3.96 to 5.72 nm and 31.56 nm up to 320.15 nm. When the temperature reached 700 °C, the outer surface of the oxide layer contained a small amount of  $\alpha$ -Al<sub>2</sub>O<sub>3</sub>, while the interior consisted of a large amount of  $\gamma$ -Al<sub>2</sub>O<sub>3</sub>, indicating that the conversion of  $\gamma$ -Al<sub>2</sub>O<sub>3</sub> to  $\alpha$ -Al<sub>2</sub>O<sub>3</sub> occurred from the inside out.

**Keywords** Aluminum particle · Physicochemical characteristics · Thermal oxidation characteristics · Oxide layer thickness · Crystalline transformation and distribution

## Introduction

Micro-aluminum particles are frequently used energetic materials that have found applications in solid propellants [1, 2]. Their popularity is due to their ability to increase the burning temperature to improve the specific impulse of the motor [3] and also due to the plentiful aluminum resources and non-toxic nature of their combustion products [4]. Since 1950s, scholars from various countries have been involved in the research on aluminum particles [1, 5, 6].

Until now, there is no systematic reaction mechanism or model to characterize the reaction process of aluminum

particles under different conditions. Due to the controllability of reaction, many scholars have extensively studied the reaction mechanism of aluminum particles by thermal analysis and have revealed the two main types of mechanisms involved—diffusive oxidation and melt dispersion oxidation. Trunov [7] considered that the oxidation process of aluminum particles was mainly affected by the migration rate of internal Al ions and external O ions. The particle size was the main factor affecting the oxidation rate, and the reaction rate increased with the decrease in particle size. Zhang and Rai [8, 9] found by microscopic observation that the aluminum sample formed a cavity coated by compact oxide layer after oxidation, which confirmed that the oxidation reaction had occurred on the surface of oxide layer. Levitas [10] reported that when the heating rate was high, the aluminum particles followed the melt dispersion oxidation mechanism rather than the diffusive oxidation mechanism. The volume expanded after the internal aluminum melted, and due to the pressure difference, the

✉ Jianzhong Liu  
jzliu@zju.edu.cn

<sup>1</sup> State Key Laboratory of Clean Energy Utilization, Zhejiang University, Hangzhou 310027, China

<sup>2</sup> Institute of Aerospace Science and Technology Corporation, Xi'an 710000, China

oxide layer was broken. Finally, the aluminum droplets were sputtered outside, and small size alumina particles were formed. However, Levitas [10] reported on the influence of and thickness of oxide layer by experiments. Increasing the thickness of the oxide layer and the active aluminum radius was found to improve the reaction rate and flame propagation speed.

The main factors affecting the reaction are particle size distribution and oxidation atmosphere. Trunov [11] pioneered the use of thermal analysis from room temperature to 1500 °C to observe the reaction process of aluminum particles. Four crystal changes were observed. The transformation process from amorphous alumina,  $\gamma$ -Al<sub>2</sub>O<sub>3</sub>,  $\delta$ -Al<sub>2</sub>O<sub>3</sub>,  $\theta$ -Al<sub>2</sub>O<sub>3</sub>, to the final state  $\alpha$ -Al<sub>2</sub>O<sub>3</sub> on the surface was studied. Sun [12] studied the reaction mechanism of nano- and micron-aluminum particles in CO<sub>2</sub> and found that the reaction mechanism of aluminum particles in CO<sub>2</sub> still obeys the diffusive oxidation mechanism. The CO<sub>2</sub> diffused into particles and reacted with Al. The transformation of amorphous alumina,  $\gamma$ -Al<sub>2</sub>O<sub>3</sub> and  $\alpha$ -Al<sub>2</sub>O<sub>3</sub>, occurred on the surface of nano-aluminum particle; however, micro-aluminum displayed a cracking phenomenon in the oxide layer. Rufino [13] employed the thermal analysis method with a variety of physicochemical characterization test to study the effect of particle size and atmosphere on the oxidation process of aluminum particles. The thickness of oxide layer was irrelevant to the particle size during the oxidation process, and the coagulation and agglomeration of particles under the oxidation conditions were weaker than that under inert atmosphere.

There is no systematic characterization method to analyze the physicochemical properties of micro-aluminum particles comprehensively, especially to test the oxide thickness. Because of the multiple crystalline form transformation during the reaction process, the thickness and the molecular structure changed which caused the ion migration to change. The studies to date on the oxidation mechanism of micron-sized aluminum particles in air and carbon dioxide atmosphere are not sufficient or satisfactory. Most studies of oxidation mechanism are mainly focused on the transformation of the crystalline, and the crystalline transformation is only tested by XRD, but the specific morphological structure, thickness and distribution rules of oxide layer are not studied in depth. In this study, the relevant physicochemical properties were tested by scanning electron microscopy, energy dispersive spectroscopy, nitrogen adsorption instrument, laser particle analyzer, X-ray diffraction and inductively coupled plasma atomic emission spectrometry. A mathematical model to calculate the specific surface area and active aluminum content was established. The thermal oxidation characteristics of the samples were studied in air, and the thermogravimetry (TG), differential thermogravimetry (DTG) and

differential scanning calorimetry (DSC) curves of the samples in the range of 200–1100 °C were obtained. The physical and chemical properties of the oxidized products were tested, and the formation mechanism of the oxide layer was studied at different temperatures.

## Materials and methods

### Materials

The aluminum powder was purchased from Shuitian Technology Co., Ltd., Shanghai, China.

### Devices and methods

The scanning electron microscopy (SEM) images were taken by a Hitachi SU-70 field emission SEM, after gold sputtering for 2 min. Particle size distribution was analyzed by a laser particle analyzer (BT-9300ST, BaiTe Co., China), with anhydrous alcohol as the dispersant. The crystal structure analysis of the sample was performed on the X-ray diffractometer (XRD) (X'Pert Pro, Panalytical Co., Netherland), and the diffraction angle was set to 10°–90°. Adsorption–desorption measurements were performed at -196 °C using nitrogen with Autosorb-1-C from Quantachrome, USA. Elemental analysis was performed using an inductively coupled plasma atomic emission spectrometer (ICP–AES, ThermoScientific XII, USA). A double beam ion focusing micro/nano-processing instrument (FIB) (Quanta FEG 3D, FEI Co., USA) was used to pretreat the sample and obtain ultrathin sections. The aluminum particle was loaded on the silicon slice and cut by the ion beam under the protection of Pt. After the process, a slice of the sample was obtained which was only a few hundreds of nanometers thick. The slice was extracted and fixed on the Mo screen and finally cut to 100 nm for studying its morphology. The microscopic morphology of the samples was examined by transmission electron microscope (TEM) (Tecnai G2 F20, FEI Co., USA).

The thermal analysis experiments were performed on a Q600 thermogravimetric analyzer (TA Co., USA). The mass loss and heat release of the samples were studied from 200 to 1100 °C. Under nitrogen atmosphere, the condensed products from heating up to 550, 700 and 1100 °C were collected separately. The heating rate of the instrument was set at 10 °C min<sup>-1</sup>, and the reaction gas was air at a constant gas flow of 100 mL min<sup>-1</sup>. Approximately 5 mg of the samples was placed in the crucible for each TG experiment.

## Results and discussion

### Physicochemical characteristics

#### Micromorphology and particle size distribution

The microstructure of the samples was observed by scanning electron microscope. As shown in Fig. 1, the samples were spherical in shape, and a few small particles were attached to the surface. Figure 2 shows the particle size distribution of the samples tested by laser particle size analyzer. The particle size distribution was between 0.5 to 16  $\mu\text{m}$ , and the average particle size was 5.366  $\mu\text{m}$  with the standard deviation of 0.242  $\mu\text{m}$ , which indicated that the size distribution was narrow.

#### Oxide layer

The occurrence form of aluminum element is given in Fig. 3. The diffraction pattern of the samples has five peaks at  $38.5^\circ$ ,  $44.7^\circ$ ,  $65.1^\circ$ ,  $78.2^\circ$  and  $82.4^\circ$  corresponding to Al. Only the characteristic peaks of aluminum were observed, but no aluminum oxide was detected, which does not mean that there was no oxide in the sample. According to the elemental composition of the sample shown in Table 1, a certain amount of O is present in the sample, which suggests that the samples in the initial stage contained aluminum oxide in the form of amorphous alumina which cannot be measured by X-ray diffraction. In order to confirm this assumption, ultrathin sections of the samples were obtained by using a FIB system. The ultrathin sections were then studied by TEM, and the images are shown in Fig. 4. According to the contrast of the structure, the sample can be clearly divided into three parts. In order to determine the specific components of each layer, the elements were analyzed in ultrathin sections by EDS. The upper layer mainly consisted of aluminum element, and the lower layer was mainly made up of silicon element. There was a third small layer between these two layers which contained aluminum and oxygen elements, and the content of Al and O was about 1:1 (similar to that in alumina).

**Fig. 1** SEM characterization of sample **a**  $5000\times$ , **b**  $\times 10,000$

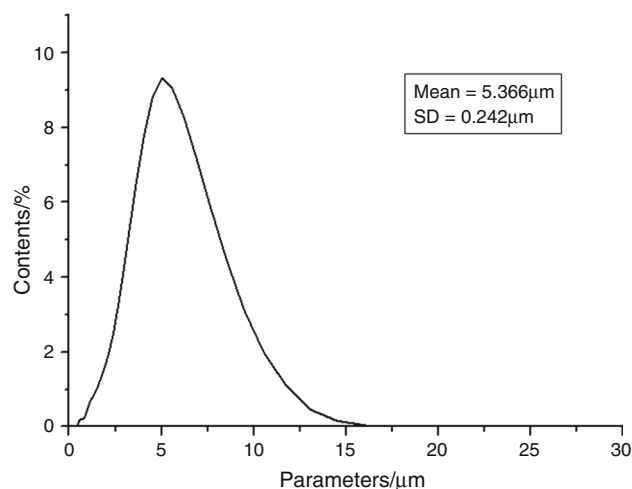
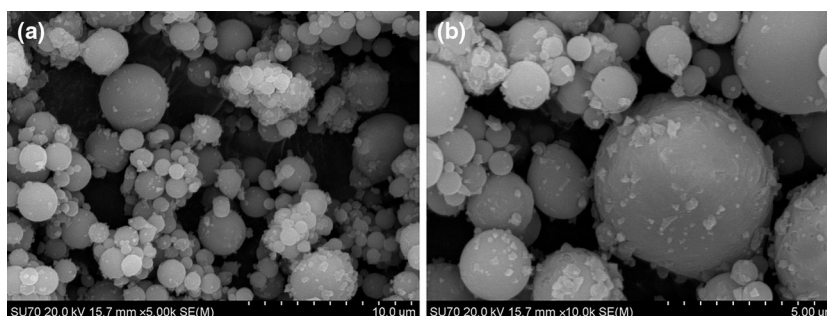


**Fig. 2** Particle size distribution of sample

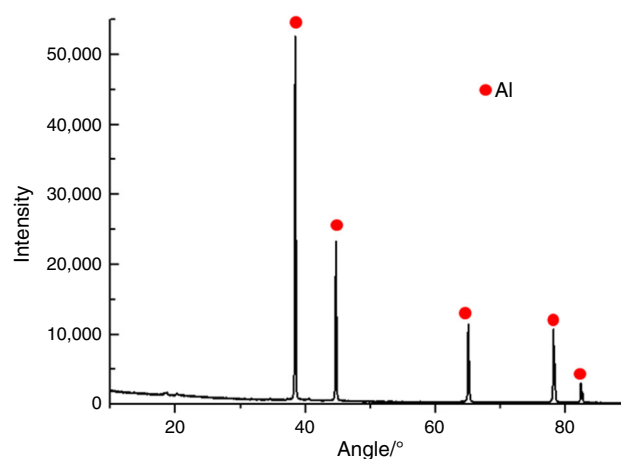
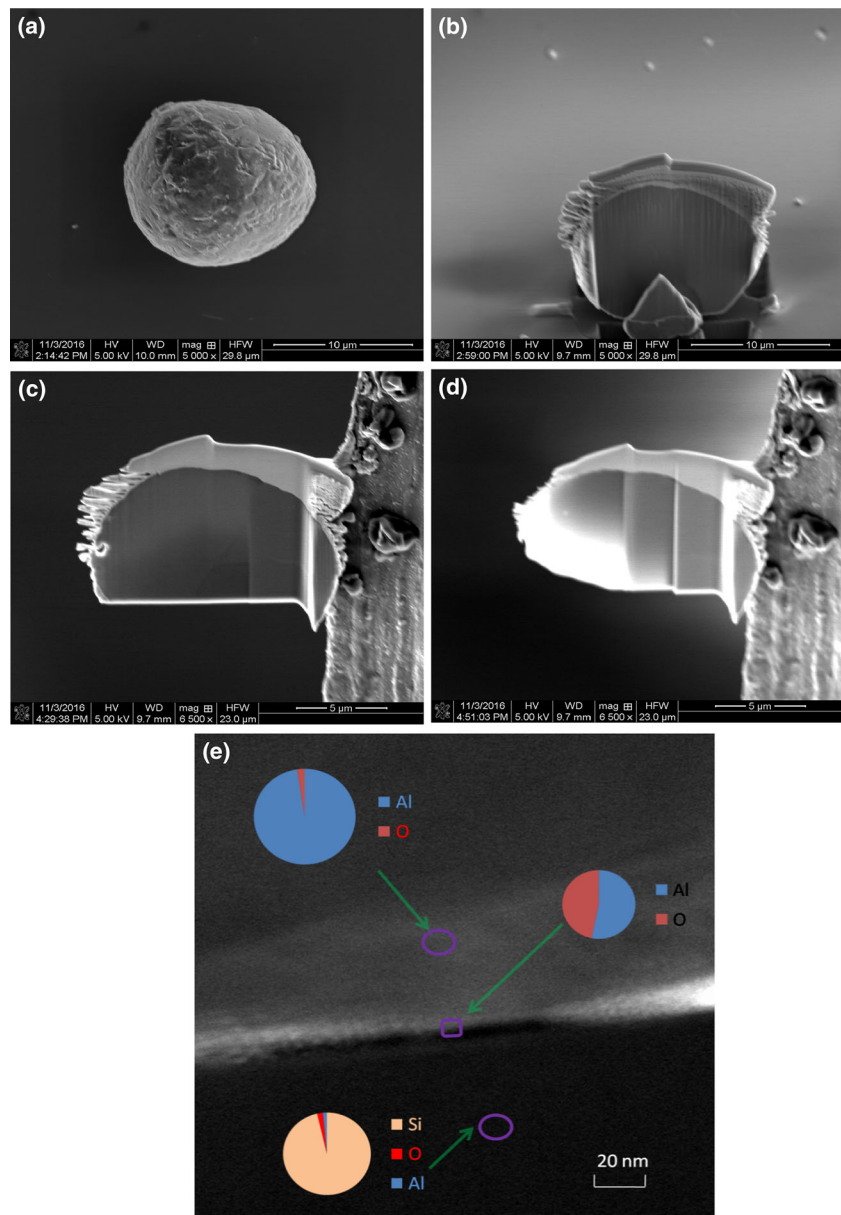


**Fig. 3** XRD pattern of the sample

**Table 1** Elemental composition of the sample

	Al/mass%	O/mass%	Others/mass%
Sample/%	91.32	5.99	2.69

**Fig. 4** Process of FIB treatment (a–d) and the ultrathin sections under TEM (e). **a** The aluminum particle was loaded on, **b** the particle was cut by the ion beam silicon slice under the protection of Pt, **c** the slice was extracted and fixed on, **d** the slice was cut to 100 nm finally the Mo screen, **e** the ultrathin sections under TEM



Therefore, the upper section was active aluminum, the lower section was silicon slice, and the oxide layer was between them. Ten consecutive positions were measured as shown in Fig. 4e. The average thickness of the oxide layer was  $3.96 \pm 0.12$  nm, indicating that the initial oxide layer of the sample was about 3.96 nm in thickness, which is consistent with the results of Rufino [13]. Therefore, it can be concluded that the aluminum particle was composed of an inner aluminum core and an outer layer of amorphous alumina layer with the thickness of about 3.96 nm [14, 15].

### Mathematical model and verification

Here, a mathematical model was developed to calculate the specific surface area and active aluminum content of the sample, and the calculated values were verified through the corresponding experimental results.

In the mathematical model, it was assumed that the sample had a regular spherical shape. The specific surface area and active aluminum content of the sample can be calculated by the particle size distribution and the thickness of the oxide layer using the following two equations, respectively:

$$a = \frac{\Sigma(D/2)^2}{\frac{1}{3}\Sigma[(\rho_1 - \rho_2) \times ((D/2) - \delta)^3 + \rho_2 \times (D/2)^3]} \quad (1)$$

$$w = \frac{\Sigma\rho_1 \times ((D/2) - \delta)^3}{\Sigma[(\rho_1 - \rho_2) \times ((D/2) - \delta)^3 + \rho_2 \times (D/2)^3]} \quad (2)$$

where  $a$  is the specific surface area of the sample,  $\text{m}^2 \text{g}^{-1}$ ;  $w$  is the content of the active aluminum, %;  $D$  is the particle size, nm;  $\rho_1$  and  $\rho_2$  are the density values of aluminum and amorphous alumina,  $2.7$  and  $3.05 \text{ g cm}^{-3}$ , respectively; and  $\delta$  is the thickness of oxide layer,  $3.96 \text{ nm}$ .

To obtain experimental verification, the specific surface area of the sample was also measured by nitrogen adsorption–desorption measurements, and the adsorption–desorption curve is shown in Fig. 5. The adsorption isotherms of the sample belong to type 2 of the IUPAC classification [16], that is to say, the sample is a non-porous or porous material. Based on SEM results, the sample was actually found to be a non-porous material. The specific surface area of the sample can be obtained by BET equation. The active aluminum content in the sample can not only be obtained through simple calculations, but can also be obtained experimentally by EDS test back-stepping or ICP method. Both these methods have been used in this

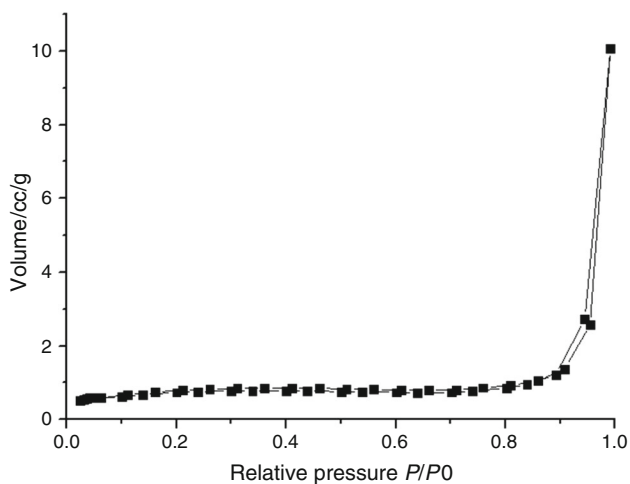


Fig. 5 Adsorption–desorption curve of the sample

Table 2 Calculated and measured values of the specific surface area and active aluminum content

	Sample
$a/\text{m}^2 \text{g}^{-1}$ (Calculated through equation)	2.522
$a/\text{m}^2 \text{g}^{-1}$ (Adsorption measurements)	2.662
$w/\%$ (Calculated through equation)	79.44
$w/\%$ (EDS measurements)	84.58
$w/\%$ (ICP measurements)	84.90

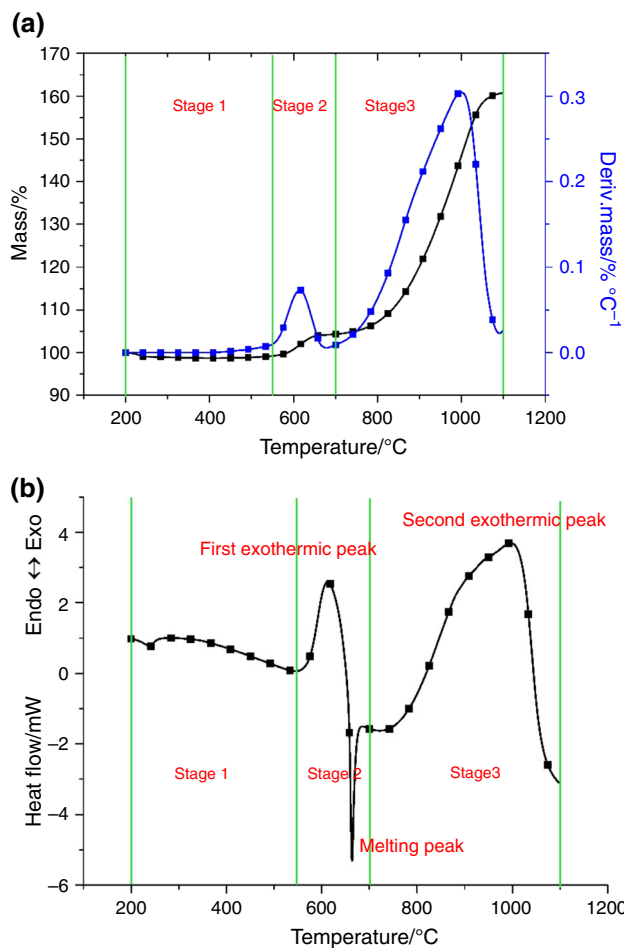
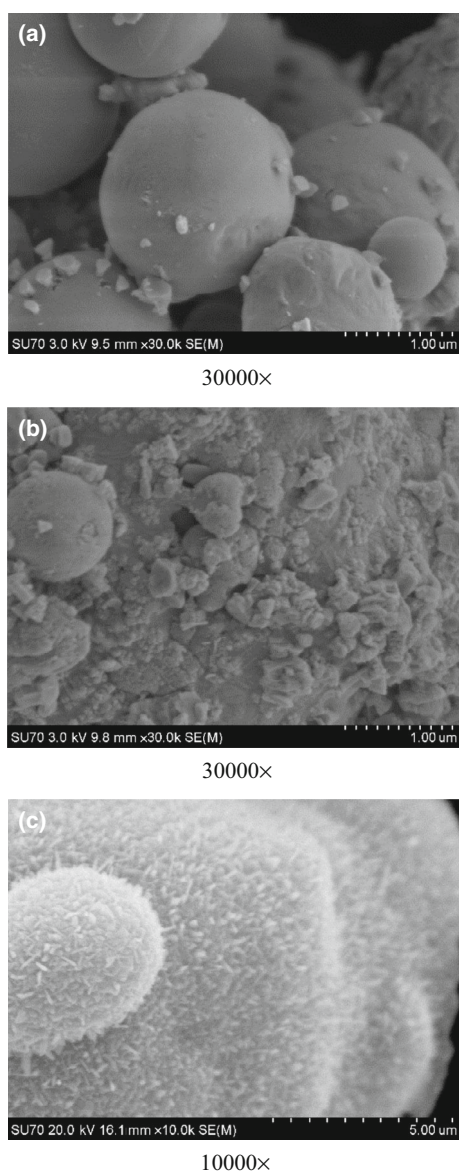


Fig. 6 Thermal analysis curves. a TG/DTG curves, b DSC curves

work to obtain the Al content. The active aluminum was dissolved by acidic copper sulfate solution, and the Al element in the solution was tested by ICP.

Table 2 shows the calculated values and experimental values of the specific surface area and the content of active aluminum. The mathematical model using the thickness of the oxide layer and the particle size distribution was quite accurate. The calculated value was in good agreement with the measured value, and the error was less than 10%. This result indicates that the specific surface area and the content of active aluminum of the sample can be accurately obtained by the size distribution and thickness of the oxide layer. It can be seen from Table 2 that the calculated value was slightly lower than the measured value. The main reason for this difference is that the actual sample was not perfectly spherical and the surface was not completely smooth.





**Fig. 7** SEM images of oxidized products at different temperatures. **a** SEM images of oxidized products at 550 °C, **b** SEM images of oxidized products at 700 °C, **c** SEM images of oxidized products at 1100 °C

### Thermal oxidation characteristics

Figure 6 shows the TG, DTG and DSC curves of the sample in the range of 200–1100 °C. As shown in Fig. 6a, the oxidation process can be divided into three stages, which is consistent with the experimental results of Trunov et al. [12]. In the temperature range of 200–550 °C, a small mass loss process was observed. The main cause of the loss was the desorption of the surface water and the removal of hydroxyl (OH) groups from the amorphous alumina [13]. The smaller the particle size, the larger the specific surface area, and the more obvious the mass loss

process. The slow oxidation process was due to the slow Al and O migration rate under low temperature. In the range of 550–700 °C, there was a step-type oxidation process, and the mass increased by 5%. When the temperature was higher than 700 °C, there was a process of accelerated mass gain of the sample.

In Fig. 6b, no endothermic or exothermic peak could be observed below 550 °C. When the temperature reached 550–650 °C, an obvious exothermic peak was recorded and at 650–700 °C, there was a strong absorption peak, whose position matched the melting point of aluminum (660 °C). Above 700 °C, an ongoing exothermic oxidation reaction occurred and the DSC curve showed an exothermic peak. This phenomenon showed that the initial reaction of the sample was earlier than the melting of the internal aluminum core, i.e., the O entered through the oxide layer into the interior of the particle and started reacting with the internal aluminum core before the internal aluminum began melting. As seen from Fig. 6, the static oxidation reaction process of micro-aluminum particle was mainly divided into three stages: (1) the sample experienced a slow heat release process before the temperature reached the initial reaction temperature; (2) the sample underwent an obvious exothermic reaction and then reached the melting point at 660 °C; (3) the sample rapidly oxidized and the DSC curve showed a broad exothermic peak.

Thermal oxidation characteristics are essential parameters to characterize the thermal reaction of the sample. The  $\Delta m$  term represents the maximum mass gain of the sample, and  $m_{de}$  is the maximum mass loss before the initial reaction. From Fig. 6a, it was found that the maximum mass gain reached 60.7% at 1100 °C, and the mass loss was 1.30% before the initial reaction. During the thermal reaction process, the mass gain was caused by the diffusion of O into the particle to form alumina, so the thermal oxidation efficiency can be obtained by calculating the increase in mass of O. The following equation is used for this purpose:

$$\eta = \frac{9 \times (\Delta m + m_{de})}{8 \times (1 - m_{de}) \times w} \quad (3)$$

When the temperature increased to 1100 °C, the thermal oxidation efficiency reached to 83.24%.  $T_i$  is the initial reaction temperature of the sample, which can be obtained by tangent method [17] using TG/DTG curve. It can also be acquired from the DSC curve. The final initial reaction temperatures were 562.09 and 559.73 °C by these two methods [18], and the error was less than 1%.

### Crystalline transformation and distribution

In order to further study the crystalline transformation observed in air atmosphere, the sample was heated to 550,

700 and 1100 °C, respectively. Figure 7 shows the microstructures of the sample and its oxidized products. There were obvious differences in the microstructures at the different temperatures.

When heated to 550 °C, the morphology of the oxidized sample was similar to that of the original sample (Fig. 7a). The sample still showed a relatively regular spherical structure, there were some white convex particles, and the surface was found to be compact. This result indicated that the surface morphology of the sample did not change significantly and the oxide layer did not become crystalline when heated up to 550 °C. The oxide layer was still amorphous alumina. When the temperature rose to 700 °C, the morphology of the sample showed some changes for the first time, as shown in Fig. 7b. The surface was no longer smooth and compact, and small particles of diameter less than 0.5 μm were attached to the surface [19]. It could be seen that the surface of the oxide layer structure was loose and discontinuous. At the same time, the first change occurred in the crystallinity of the oxide layer. With the increase in temperature, the surface morphology of the sample changed again at 1100 °C, and the surface of the sample displayed an acicular structure, as shown in Fig. 7c.

As shown in Fig. 8, when the sample was heated to 700 and 1100 °C, the oxide layer ruptured, and the internal aluminum completely overflowed outside. However, the particle remained intact at 550 °C, which indicated that the particle rupture occurred after the initial reaction and melting of the internal aluminum. This phenomenon also indirectly illustrated that the breakage of aluminum particle in the thermal reaction process was caused by internal expansion of molten aluminum.

In order to confirm the crystalline transformation of the oxide layer, the sample was analyzed by XRD at different temperatures. The results are shown in Fig. 9. At 25 and 550 °C, only the Al diffraction peak was observed. As mentioned in Sect. 3.1, there was still a small amount of amorphous alumina present. When the temperature was lower than 550 °C, the Al element speciation was aluminum and amorphous alumina. However, when the temperature was raised to 700 °C, the  $\gamma$ -Al<sub>2</sub>O<sub>3</sub> phase appeared

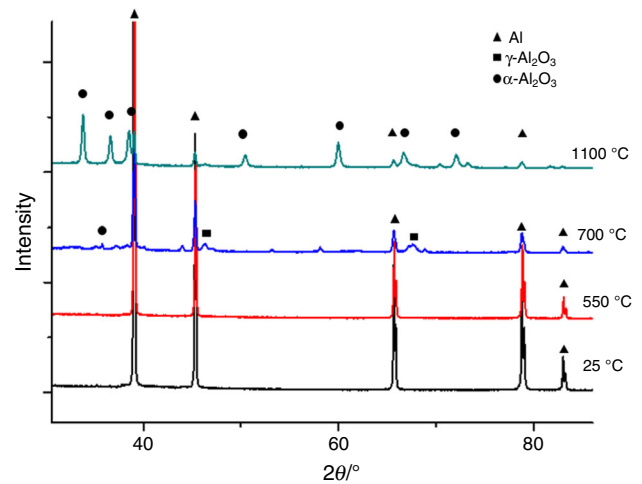
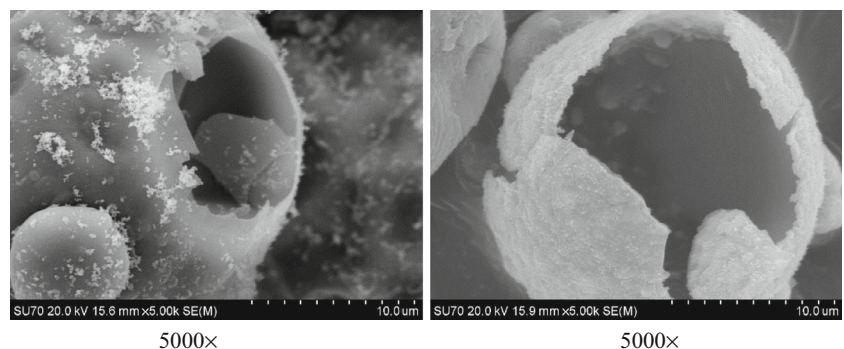


Fig. 9 XRD curves of the sample at different temperatures

in the oxide layer, which indicated that the amorphous alumina transformed to  $\gamma$ -Al<sub>2</sub>O<sub>3</sub>, which corresponds to the results observed in Fig. 7b. When the temperature reached 1100 °C, the diffraction peak of Al almost disappeared, indicating that the aluminum was completely oxidized. Moreover, the  $\gamma$ -Al<sub>2</sub>O<sub>3</sub> phase disappeared and was replaced by a large amount of  $\alpha$ -Al<sub>2</sub>O<sub>3</sub>. This result is consistent with the results shown in Fig. 7c.

During the thermal reaction process, not only the crystallinity of the oxide layer changed, but also the thickness of the oxide layer showed a large increase. In order to explore the oxide layer thickness and the distribution of different crystalline phases after heat treatment, FIB was employed to pretreat the oxidized products and TEM was used to observe the microstructure. Figure 10 shows the microstructures of the oxidized particle treated at different temperatures. During the slicing process, the sample was loaded on a single crystal silicon wafer. According to the different contrast, the sample was observed to have three parts. Region 1 and region 3 were homogeneous structures, while region 2 was a continuous but inhomogeneous structure. The energy spectrum was used to determine the elemental composition of the three regions, as shown in

Fig. 8 Partial SEM images of oxidized products at 700 and 1100 °C



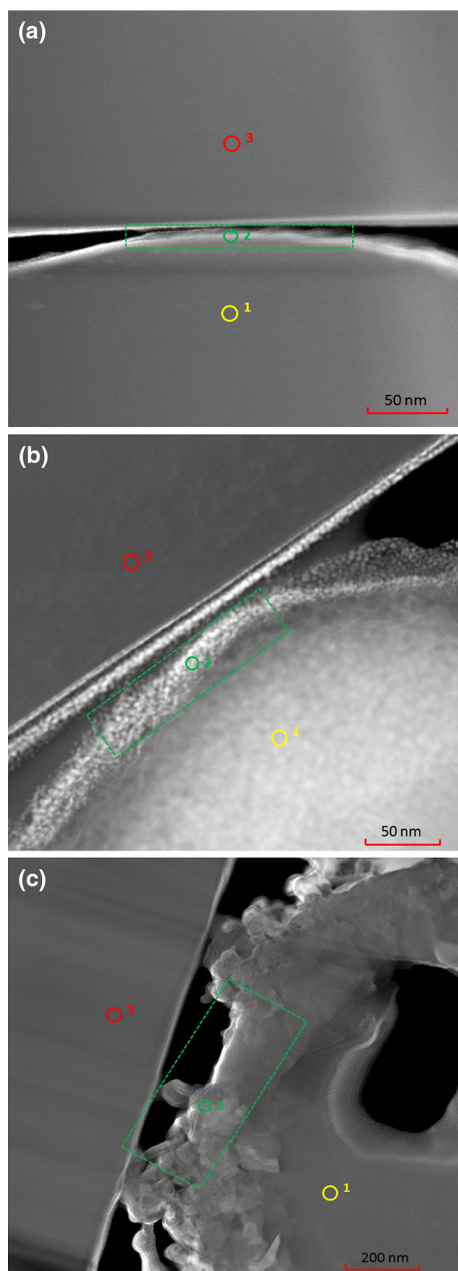


**Fig. 10** TEM images of ultrathin sections of the oxidized products at different temperatures. **a** 550 °C, **b** 700 °C, **c** 1100 °C

Table 3. It can be found that the region 1 was almost pure aluminum, and the region 3 was silicon. Region 2 was composed of Al and O elements with a mass ratio close to 1:1 (the content of Al and O in aluminum oxide is close to 1:1), and therefore, this area was the oxide layer of the sample.

From the TEM images, it can be seen that there are obvious differences in the microstructures of the oxide layer at different temperatures. At 550 °C, the oxide layer was almost the same as that of the original sample. Ten positions were selected to measure the oxide layer

thickness, and the average value was about 5.72 nm, and it was increased by 1.76 nm relative to the initial film thickness of 3.96 nm. This result also indirectly explained why the mass increase was very small at the beginning of the reaction, i.e., O diffused through the amorphous oxide layer into the Al core, and the reaction rate was slow due to low temperature, so the mass gain was very small. No crystalline transformation occurred. When the temperature was raised to 700 °C, the oxide layer was no longer uniform, and the thickness was greatly increased. The average oxide thickness increased to 31.56 nm. Over a narrow temperature range (550–700 °C), the oxide layer rapidly thickened, which explained the rapid increase in mass. When the temperature increased to 1100 °C, the morphology of oxide layer was changed greatly, and appeared irregular. The average thickness increased significantly to about 320.15 nm. There was a large cavity inside and a little Al nearby, which illustrated that the reaction followed the diffusion oxidation mechanism. The Al diffused outward, the O diffused inside, and finally, the oxide layer became thicker. The phenomenon indirectly confirmed that the diffusion oxidation mechanism occurred in aluminum particle during thermal oxidation process [20, 21].

According to the tests above, the high-resolution TEM images of the FIB ultrathin sections can only be used to qualitatively analyze the microstructure and measure the oxide layer thickness. The crystallinity of the sample can be tested by XRD only, and the distribution of different crystalline phases cannot be tested. For a more in-depth analysis of the specific distribution of different crystalline phases in the thermal oxidation process, Fig. 11 shows the high-resolution images of the oxide layer (green box in Fig. 10b, c), and the types of crystalline phases could be distinguished by measuring the crystal lattice fringes interval. From Fig. 11, it was found that there were two kinds of crystal lattice fringes intervals, which were 2.800 and 0.997 nm. From the standard PDF card, it was found that the value of 2.800 nm represented the  $\gamma$ -Al<sub>2</sub>O<sub>3</sub> while the value of 0.997 nm indicated  $\alpha$ -Al<sub>2</sub>O<sub>3</sub>. So, at 700 °C, there were a large number of  $\gamma$ -Al<sub>2</sub>O<sub>3</sub> particles located on the inner edge, and the outer edge contained a small amount of  $\alpha$ -Al<sub>2</sub>O<sub>3</sub>. The results showed that during the reaction process, transformation of  $\gamma$ -Al<sub>2</sub>O<sub>3</sub> to  $\alpha$ -Al<sub>2</sub>O<sub>3</sub> occurred from the inside out. When heated up to 1100 °C, the entire oxide layer was composed of  $\alpha$ -Al<sub>2</sub>O<sub>3</sub>, and there was no  $\gamma$ -Al<sub>2</sub>O<sub>3</sub> left.

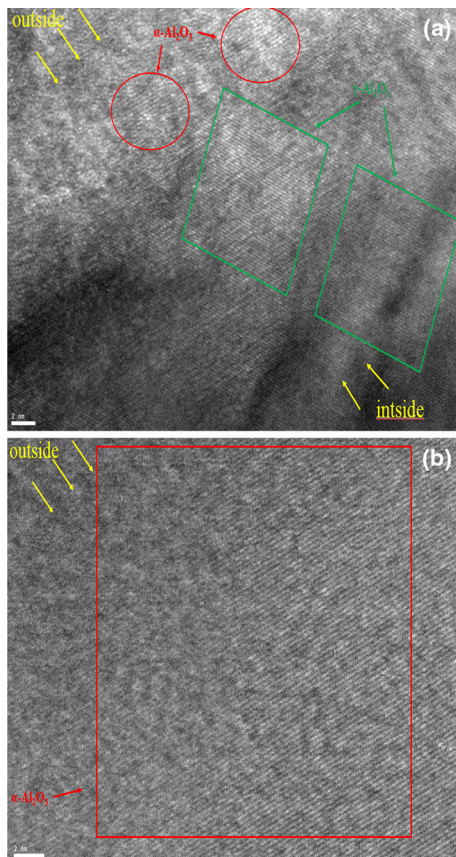
## Conclusions

In this work, the physical and chemical properties of micron-aluminum particle were evaluated and especially the oxide layer, the oxidation mechanism, oxide layer



**Table 3** Elemental composition at different sections

Temperature/°C	550			700			1100		
	Al	O	Si	Al	O	Si	Al	O	Si
Section 1/%	98.87	0.55	0.57	99.16	0.11	0.71	98.94	0.73	0.32
Section 2/%	53.54	45.63	0.83	53.78	46.02	0.20	54.96	45.00	0.04
Section 3/%	1.08	0.64	98.27	1.03	0.76	97.84	0.45	0.22	98.91

**Fig. 11** TEM images of oxide layer at **a** 700 °C and **b** 1100 °C

transformation and crystalline distribution were investigated. The main highlights of this work are summarized below.

1. The physical and chemical properties of micron-aluminum particle were evaluated by SEM, laser particle size analyzer, XRD and ICP-AES. The thickness of the oxide layer was about 3.96 nm, and the relationship between specific surface area and active aluminum content was established. The error of the calculated values of specific surface area and active aluminum content was less than 10%.
2. The thermal oxidation characteristics of the sample were studied by thermal analyzer. The process was divided into three reaction stages: (1) the sample experienced a slow release process before the temperature reached the initial reaction temperature; (2) the sample underwent an obvious exothermic reaction and then reached the melting point at 660 °C; (3) the sample was rapidly oxidized, and the DSC curve showed a wide exothermic peak. The thermal oxidation efficiency was 83.24% when the temperature was increased to 1100 °C.
3. The oxidized products were analyzed using SEM, XRD, FIB and TEM. With the increase in treatment temperature, dramatic crystalline changes occurred on the surface of the sample: amorphous alumina,  $\gamma$ - $\text{Al}_2\text{O}_3$ ,  $\alpha$ - $\text{Al}_2\text{O}_3$ , and the oxide layer thickness increased from 3.96 to 5.72 nm initially, then to 31.56 nm and finally, up to 320.15 nm. When the temperature reached 700 °C, the outer surface of the oxide layer had only a small amount of  $\alpha$ - $\text{Al}_2\text{O}_3$ , while the interior mostly consisted of  $\gamma$ - $\text{Al}_2\text{O}_3$ , indicating that the conversion of  $\gamma$ - $\text{Al}_2\text{O}_3$  to  $\alpha$ - $\text{Al}_2\text{O}_3$  proceeded from the inside out.

**Acknowledgements** This work was funded by the National Natural Science Foundation of China (No. 51376160) and the National Natural Science Foundation of China (No. 51706057).

## References

1. Badiola C, Gill RJ, Dreizin EL. Combustion characteristics of micron-sized aluminum particles in oxygenated environments. *Combust Flame*. 2011;158(10):2064–70.
2. Cheng H, Chen X, Zhou C, et al. Research progress on combustion characteristics of aluminum particles. *J Ordnance Equip Eng*. 2010;31(3):84–8.
3. Bazyn T, Krier H, Glumac N. Evidence for the transition from the diffusion-limit in aluminum particle combustion. *Proc Combust Inst*. 2007;31(2):2021–8.
4. Pang WQ, Fan XZ. Application progress of metal fuels in solid propellants. *Chem Propellants Polym Mater*. 2009;7(2):1–14.
5. Gill RJ, Badiola C, Dreizin EL. Combustion times and emission profiles of micron-sized aluminum particles burning in different environments. *Combust Flame*. 2010;157(11):2015–23.
6. Mohan S, Furet L, Dreizin EL. Aluminum particle ignition in different oxidizing environments. *Combust Flame*. 2010;157(7):1356–63.
7. Trunov MA, Schoenitz M, Dreizin EL. Effect of polymorphic phase transformations in alumina layer on ignition of aluminium particles. *Combust Theor Model*. 2006;10(4):603–23.
8. Zhang S, Dreizin EL. Reaction interface for heterogeneous oxidation of aluminum powders. *J Phys Chem C*. 2013;117(27):14025–31.

9. Rai A, Park K, Zhou L, et al. Understanding the mechanism of aluminium nanoparticle oxidation. *Combust Theor Model*. 2006;10(5):843–59.
10. Levitas VI, Pantoya ML, Dikici B. Melt dispersion versus diffusive oxidation mechanism for aluminum nanoparticles: critical experiments and controlling parameters. *Appl Phys Lett*. 2008;92(1):11921.
11. Trunov MA, Schoenitz M, Zhu X, et al. Effect of polymorphic phase transformations in  $\text{Al}_2\text{O}_3$  film on oxidation kinetics of aluminum powders. *Combust Flame*. 2005;140(4):310–8.
12. Sun Y, Sun R, Zhu B, et al. Thermal reaction mechanisms of nano- and micro-scale aluminum powders in carbon dioxide at low heating rate. *J Therm Anal Calorim*. 2016;124(3):1727–34.
13. Rufino B, Boulc HF, Coulet MV, et al. Influence of particles size on thermal properties of aluminium powder. *Acta Mater*. 2007;55(8):2815–27.
14. Levin I, Brandon D. Metastable alumina polymorphs: crystal structures and transition sequences. *J Am Ceram Soc*. 1998;81(8):1995–2012.
15. Jeurgens LPH, Sloof WG, Tichelaar FD, et al. Thermodynamic stability of amorphous oxide films on metals: application to aluminum oxide films on aluminum substrates. *Phys Rev B*. 2000;62(7):4707–19.
16. Rouquerol F, Rouquerol J, Sing K. Adsorption by powders and porous solids. London: Academic Press; 1999.
17. Zhou H, Zhang YW, Li HP, et al. Study on thermal oxidation characteristics and kinetics of boron-based fuel-rich in different atmosphere. *J Zhejiang Univ*. 2013;47(11):1987–91.
18. Hu Z, Shi Q. Thermal analysis kinetics. Beijing: Beijing Science Press; 2001.
19. Brooks KP, Beckstead MW. Dynamics of aluminum combustion. *J Propul Power*. 1995;11(4):769–80.
20. Yunan Z, Jianzhong L, Jiahao W, et al. Progress in oxidation mechanism and combustion theory of aluminum particles. *Ordinance Mater Sci Eng*. 2017;40(2):28–35.
21. Tian R, Zhang L. Literature review of single aluminum combustion model and theoretical research. *J Ordnance Equip Eng*. 2016;7:137–43.